Hu et al. Nanoscale Research Letters (2020) 15:52
https://doi.org/10.1186/s11671-020-3277-3

Nanoscale Research Letters

NANO EXPRESS Open Access

Investigating Size-Dependent Conductive Properties on Individual Si Nanowires

X. F. Hu, S. J. Li, J. Wang, Z. M. Jiang and X. J. Yang*

Abstract

Periodically ordered arrays of vertically aligned Si nanowires (Si NWs) are successfully fabricated by nanosphere lithography combined with metal-assisted chemical etching. By adjusting the etching time, both the nanowires' diameter and length can be well controlled. The conductive properties of such Si NWs and particularly their size dependence are investigated by conductive atomic force microscopy (CAFM) on individual nanowires. The results indicate that the conductance of Si NWs is greatly relevant to their diameter and length. Si NWs with smaller diameters and shorter lengths exhibit better conductive properties. Together with the I–V curve characterization, a possible mechanism is supposed with the viewpoint of size-dependent Schottky barrier height, which is further verified by the electrostatic force microscopy (EFM) measurements. This study also suggests that CAFM can act as an effective means to explore the size (or other parameters) dependence of conductive properties on individual nanostructures, which should be essential for both fabrication optimization and potential applications of nanostructures.

Keywords: Si nanowires, Conductive atomic force microscopy, Conductive property, Size dependence, Schottky barrier height

Introduction

Silicon nanowires (Si NWs) have gained promising applications in electronic, photonic, optoelectronic and many other fields due to their high aspect ratio and unique electrical, thermoelectric and photoelectrical properties, as well as the compatibility with traditional silicon technology [1–5]. In the past decades, the researches of Si NWs have mainly focused on the growth improvements and property measurements. Many methods have been developed to prepare Si NWs, including bottom-up methods such as vapor-liquid-solid method, chemical vapor deposition, and molecular beam epitaxy [6–10] and top-down approaches using electron-beam lithography, reactive ion etching or metal-assisted chemical etching [11–16]. Among these methods, nanosphere lithography (NSL) combined with metal-assisted chemical etching (MACE) has been intensively adopted to fabricate large-area ordered arrays of vertically aligned Si NWs for its simplicity, low cost, and versatility [15–23]. The Si NWs achieved by MACE usually have very rough and even porous surfaces [18–21], which just makes them have a large specific surface area and excellent properties, leading to great application potentials in biosensors, thermoelectric devices, lithium-ion batteries, solar cells, etc. [22–24]. To realize those applications, it is essential to get a good understanding of their electrical properties. Nowadays two kinds of methods have often been applied to investigate the electrical properties of nanowires. One is carried out by ordinary macroscopic methods, which is relatively easy to do but can only provide averaged results over a large assembly of nanowires [24, 25]. The other is performed on individual nanowires with special fabricated single nanowire devices [21, 26–28], which could exclude the influence of size inhomogeneity but is not easy to achieve, especially when measuring the property dependence. Therefore, more convenient methods to study the electrical properties on individual NWs without complex nanofabrication are strongly required.

In recent decades, scanning probe microscopy (SPM)-based electrical measurements reveal themselves as powerful techniques for electrical characterizations at nanoscale [29, 30]. Among these SPM techniques, conductive atomic force microscopy (CAFM) has been successfully applied to study the conductive properties on single or individual

* Correspondence: xjyang@fudan.edu.cn
State Key Laboratory of Surface Physics, Fudan University, Shanghai 200433, China

Springer Open

© The Author(s). 2020 **Open Access** This article is distributed under the terms of the Creative Commons Attribution 4.0 International License (http://creativecommons.org/licenses/by/4.0/), which permits unrestricted use, distribution, and reproduction in any medium, provided you give appropriate credit to the original author(s) and the source, provide a link to the Creative Commons license, and indicate if changes were made.

nanostructures [30–32]. CAFM investigations on a variety of nanowires, such as ZnO, InAs, CdS, CdSe, GaAs, InAsSb, and Si NWs, have already been reported [33–38]. While most researches focused on the conductive properties of nanowires with fixed parameters, some investigations were carried out to explore the doping dependence of conductive properties [37–39]. The size dependencies of conductive properties of nanowires have been much less investigated yet. Only a few studies have been reported about the diameter-dependent conductive properties of nanowires, even not restricted to CAFM, and a considerable part of them dealt with the diameter dependence of nanowires' resistivity [25, 40–42]. For example, a couple of researches on GaN nanowires found that the resistivity was high at a critical diameter (20 ~ 80 nm, dependent on fabrication methods) and kept unchanged beyond it [41, 43], whereas other researches on Si nanowires reported that the nanowire resistivity decreased with increased diameter in the range of tens to hundreds of nanometers [40, 44]. For semiconductor nanowires with metal contacts, Schottky barrier may play an important role in their conductive properties. Therefore, except for the resistivity, the Schottky barrier should be taken into consideration in the presence of semiconductor nanowires. Several papers have focused on the diameter dependence of Schottky barrier height (SBH), but the results are not consistent. For instance, Calahorra et al. calculated the SBH by solving Poisson's equation in nanowire, and found a clear trend of increased barrier height with size reduction [45]. Similar diameter dependence was experimentally reported by Soudi et al. when investigating the diameter-dependent surface photovoltage and surface state density on ZnO single nanowire device. They found that the surface barrier height increased with the decreasing diameter (20–60 nm), which was interpreted by surface state density simulated using Poisson's equation [46]. By contrast, scanning photocurrent microscopy measurements on single Si nanowire field-effect transistors by Yoon et al. revealed a contrary dependence, that is, the barrier height decreased with the decreased diameter due to the contribution of interface states [47]. Another experimental work by Mao et al. on single Pt/ZnO nanoneedle Schottky diodes also reported the barrier height decreased with the decreasing diameter, which was explained by a joule heating effect and/or electronic inhomogeneity of interface [48]. Therefore up to now, the diameter dependence of nanowires' conductive properties has not reached a consensus yet and is far from being thoroughly understood. Especially, the size-dependent conductive properties as well as size-dependent SBH studies have not been reported on individual Si NWs fabricated by the MACE method, which have quite a rough surface for promising applications.

In this paper, periodic arrays of vertically aligned Si NWs with different diameters and lengths are prepared by the method of NSL combined with MACE. Both the diameter and length of SiNWs can be well controlled by adjusting the etching time. The conductive properties of individual Si NWs inside the array are investigated by CAFM without any further nanofabrication, which can study the size-dependent conductive properties on individual Si NWs conveniently by simply replacing the sample. The results demonstrate that the current measured on individual Si NWs is strongly dependent on the NWs' diameter and length. Si NWs with smaller diameters and shorter lengths exhibit better conductive properties. From I–V curve fitting, size-dependent Schottky barrier heights can be obtained, which is found to act as a key factor to determine the size-dependent conductive properties of nanowires. Furthermore, similar size-dependent SBH was obtained by electrostatic force microscopy (EFM) measurements. Therefore, our study not only reveals the size-dependent properties of Si NWs but also suggests that CAFM can act as an effective means to explore the size (or other parameters) dependence of conductive properties on individual nanostructures.

Materials and Methods

Materials

The Si wafers were purchased from MTI (China). The suspensions (2.5 wt% in water) of polystyrene spheres (PS, 490 nm in diameter) were purchased from Duke Scientific (USA). Acetone, methanol, sulfuric acid, hydrogen peroxide, and hydrofluoric acid for fabricating Si NWs were purchased from Sinopharm Chemical Reagent (China). Deionized water (DI, 18.2 MΩ·cm) was obtained from an ultrafiltration system (Milli-Q, Millipore, Marlborough, MA).

Fabrication of Si NWs

Vertically ordered silicon nanowire arrays are fabricated by NSL combined with MACE, which have been described in detail in previous literatures [49, 50]. The major fabrication process is scheduled in Fig. 1a. Firstly, a monolayer of polystyrene spheres (PS) with a diameter of 490 nm was self-assembled onto the chemically cleaned planar Si wafer (n-type, 0.01 Ω cm) to form a hexagonal close-packed monolayer. Subsequently, the PS covered sample was etched by reactive ion etching (RIE, Trion Technology) (50 W, 70 mTorr) with O_2 gas (20 sccm) to reduce the diameter of PS, which acted as the mask layer in the following procedures. Afterwards, a 20 nm Au film was deposited by ion sputtering onto the sample masked by the PS layer acted as a catalyst for the following MACE treatment. The sample was treated by MACE in HF (40%) and H_2O_2 (30%) mixed solution (volume ratio 4:1) at room temperature. In the MACE process, the Si surface covered with Au was effectively etched while that covered by PS (without Au) was protected, resulting in the formation of Si NWs. Finally, the remained Au layer and PS spheres

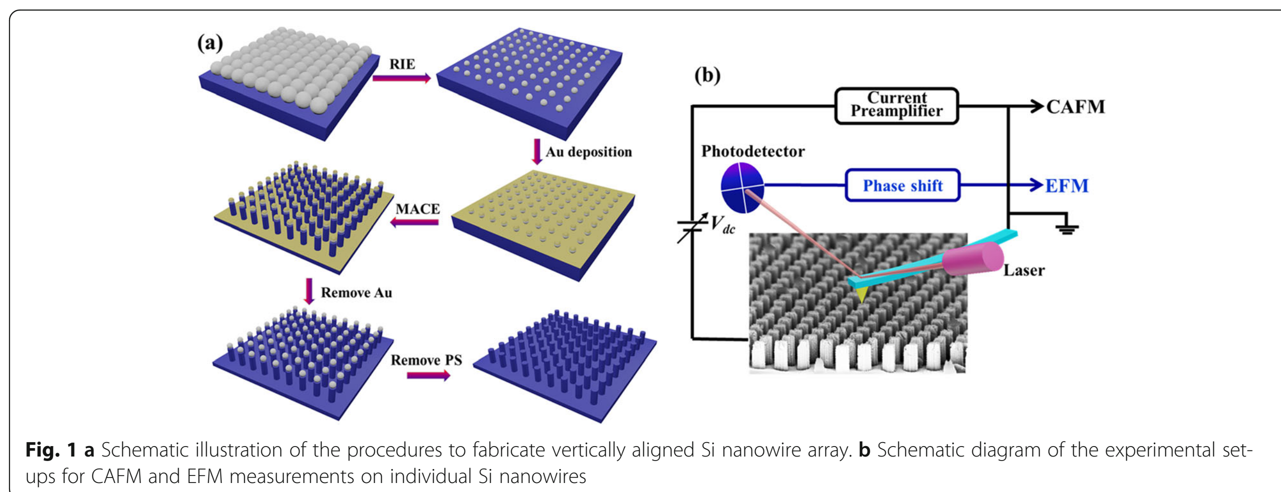

Fig. 1 **a** Schematic illustration of the procedures to fabricate vertically aligned Si nanowire array. **b** Schematic diagram of the experimental setups for CAFM and EFM measurements on individual Si nanowires

were removed by soaking the sample in KI/I_2 and tetrahydrofuran solutions, respectively. With this fabrication method, large-area periodic arrays of vertically aligned Si NW arrays can be obtained.

Characterization of Si NWs

The morphology of fabricated Si NWs was checked by scanning electron microscopy (SEM, SIGMA300) while their structural properties were investigated by Raman spectroscopy (Jobin Yvon HR-Evolution 2 system) with an excitation wavelength of 532 nm and a low power of about 1 mW.

The electrical properties of Si NWs were investigated by CAFM and EFM with a commercial SPM equipment (Multimode V, Bruker Nano Surfaces), as diagrammed in Fig. 1b. Cr/Pt-coated tips (Multi75E-G, Budget Sensors, radius approximately 25 nm) were used for both CAFM and EFM measurements. In CAFM, the conductive tip was scanned over the sample surface in contact mode with a DC bias voltage applied to the substrate while the tip was grounded, and the current between the tip and sample was measured. As the surface anodic oxidation is serious under the positive sample biases, all the current images were measured at negative sample biases. Various negative voltages ranged from − 0.5 to − 3.0 V were tested in the CAFM experiments. It was found, when the bias voltage was set below − 1.5 V, the current was too small to be detected for samples with poor conductance. While the bias voltage was set as − 2.0 V or larger, the measurements were unstable, probably due to the damage of tip and/or sample under a large electrostatic field. Therefore, the bias voltage of − 1.5 V was chosen for current image measurements. The EFM measurements were carried out on Si NWs in the two-pass mode. In the first pass, it worked in tapping mode to get the topography image, while in the second pass the tip was lifted high enough to ignore Van der Waals force. In the lifted pass, a DC voltage was added between sample and grounded tip, and the phase shift signal induced by electrostatic force was detected. All the experiments were operated in a flowing N_2 ambient for stable electrical measurements and the samples were predipped in the HF solution (5%) for 30 s to effectively reduce the influence of the oxide layer on the conductive characterization. Since the measurements were carried out immediately after HF dipping, the reformed oxygen layer should be thin enough to be penetrated by the conductive tip and its effect on the conductance is minimal.

Results and Discussions

Fabrication of Si NWs

The fabrication of large-area vertically aligned ordered Si nanowire arrays is illustrated in Fig. 1a. By changing the RIE time, the diameter of PS spheres can be reduced to desired values, and hence Si NWs with controllable diameters can be achieved. The SEM images of Si NWs obtained after 90, 120, and 150 s RIE etching are presented in Fig. 2 a, b, and c, respectively. It can be observed that the Si NWs are vertically aligned in a periodically hexagonal arrangement in a large area. These vertically aligned Si NWs have the same period of 490 nm and the same length of about 350 nm (same MACE time of 40 s). The diameters of the Si NWs in (a), (b), and (c) are around 350, 260 and 190 nm, respectively. The dependence of NWs' diameter on the RIE etching time is plotted in Fig. 2d, showing a good linear correlation. On the other hand, the length of the nanowires could be adjusted by varying the time of MACE in HF and H_2O_2 mixed solution. The cross-sectional SEM images of Si NWs after 40, 60, 80, and 100 s MACE are shown in Fig. 2e. It can be seen that the NWs' length increases from 350 to 960 nm by increasing the MACE time. Similarly, the Si NWs' length exhibits a good linear dependence on the MACE time, as shown in Fig. 2f. These results indicate that ordered Si NWs with

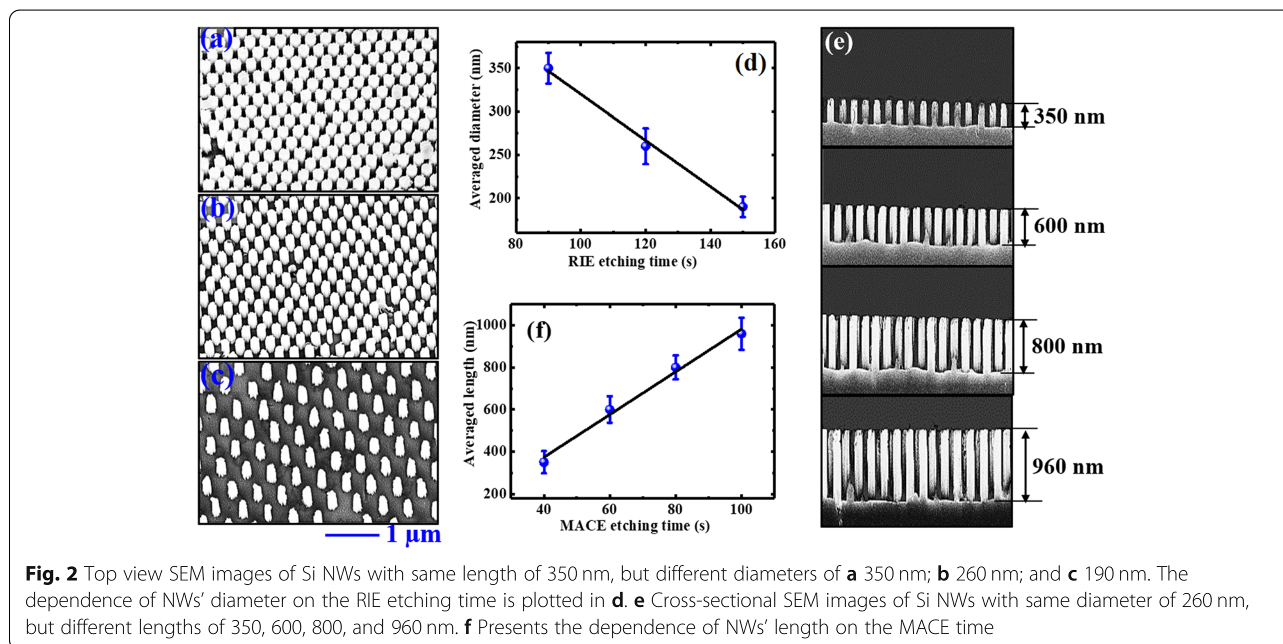

Fig. 2 Top view SEM images of Si NWs with same length of 350 nm, but different diameters of **a** 350 nm; **b** 260 nm; and **c** 190 nm. The dependence of NWs' diameter on the RIE etching time is plotted in **d**. **e** Cross-sectional SEM images of Si NWs with same diameter of 260 nm, but different lengths of 350, 600, 800, and 960 nm. **f** Presents the dependence of NWs' length on the MACE time

controllable diameters and lengths are successfully fabricated by the method of NSL combined with MACE.

From the SEM images, it can be also found that the Si NWs have a very rough surface after chemical etching, and their sidewall surface is especially rough. To check the microstructure of the surface layer as a function of diameter and length, Raman spectra were measured on both bulk Si and Si NWs with different diameters and different lengths. Each spectrum was normalized by using the maximum peak intensity at 520 cm^{-1}, and the results for different diameters and different lengths were shown in Fig. 3 a and b, respectively. The spectrum of

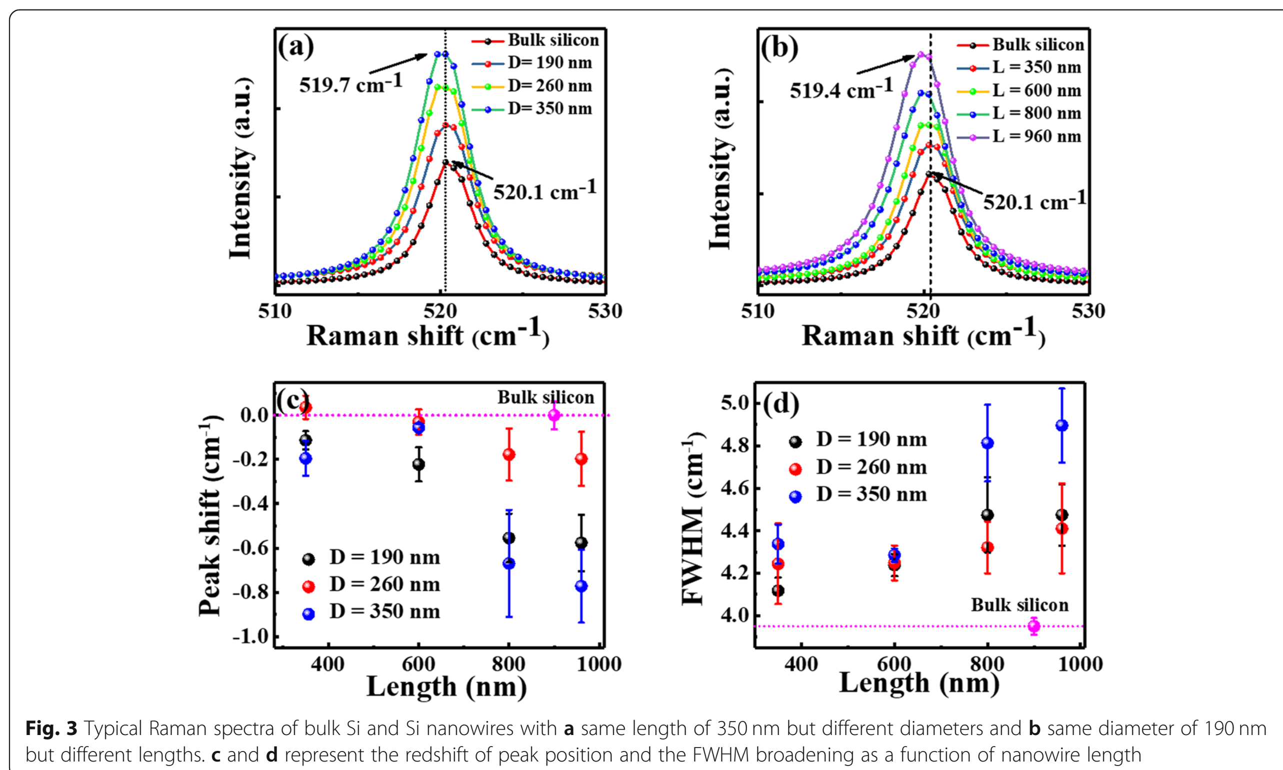

Fig. 3 Typical Raman spectra of bulk Si and Si nanowires with **a** same length of 350 nm but different diameters and **b** same diameter of 190 nm but different lengths. **c** and **d** represent the redshift of peak position and the FWHM broadening as a function of nanowire length

bulk silicon shows a sharp peak locating at ~520.1 cm^{-1}. Both the redshift of peak position and broadening of peak width (termed with full-width at half-maximum, FWHM) can be observed on Si NWs, as plotted in Fig. 3 c and d, correspondingly. The peak redshift and broadening are rather small for nanowires with short lengths of 350 and 600 nm and become relatively obvious as the nanowire length increases to 800 nm and above. Such Raman peak redshift and broadening are sometimes attributed to the changes in dopant level or crystalline content. According to the previous literatures [5, 51], for the Si NWs fabricated by the same MACE method, the doping concentration could possess the same doping level as the starting wafer. Due to equipment limitations, we were unable to confirm this result. On the other hand, although these Si NWs have a rough surface, previous literatures found that the Si NWs fabricated by the MACE method could mainly keep their crystal structures for both n- and p-doping and both light and heavy doping [5, 51, 52]. Only a thin amorphous layer was observed on the wall surface of the NWs. Similar results were obtained on Si NWs with different diameters and lengths by different groups. As such, it could be assumed the Si NWs fabricated by the MACE method can keep their dopant level and crystalline content almost unchanged as their bulk counterpart, except the thin surface layer.

Therefore, the Raman peak shift and broadening are most probably induced by the nanowires' damaged rough surface [53]. There are several papers reported the Raman results of Si NWs fabricated by the same MACE method. For example, Feser et al. found that the significant peak broadening at 520 cm^{-1} increased with MACE time and attributed this peak broadening to the crystal disorder (e.g., clusters of point defects) induced by the etching process [23]. Lajvardi et al. found that Raman redshift increased with the MACE time, i. e. the TO Raman peak was located at 521.1 cm^{-1} for bulk Si and shifted to 518.7 cm^{-1} for 80-min etched samples, respectively [54]. They stated that the origin of the Raman shift may be due to the formation of Si nanocrystals on the wall of the nanowire. Lin et al. observed that the TO Raman peak shifted from 520 to 516 cm^{-1} when the NWs' length increases from 0 (bulk Si) to 2.73 μm, while the peak width was broadened from 3 to 9 cm^{-1} with increasing NWs' length from 0.19 to 2.73 μm [55]. They thought that the Raman peak broadening was dominated by the phonon-strain interaction and the Raman peak shift was proved to be proportional to the strain-induced surface lattice distortion. Since the strain induced by HF etching increased with the NWs' length (more etching time), both the Raman peak redshift and broadening increased with the increasing NWs' length. In our case, from the Raman spectra as shown in Fig. 3 a and b, we can find that the TO Raman peak shifts from 520 to 519.4 cm^{-1} when the NWs' length increases from 0 (bulk Si) to 960 nm, while the FWHM is broadened from 4.41 to 4.47 cm^{-1} as NWs' length increases from 350 to 960 nm. We prefer this length-dependent Raman peak shift and broadening are originated from the damaged surface (strain or disorder). However, due to the very small variation in both redshift and peak broadening for nanowires with different diameters and different lengths (< 1.0 cm^{-1}), the change of strain/disorder with size can be considered minimal. So the strain/disorder may modify the NWs' conductance, but its influence on the size dependence of conductance is not concerned in the next sections.

Conductive Property Measurements on Single Si NWs

The conductive properties of Si NWs are measured by CAFM on individual NWs with different diameters and lengths. Typical topography images of the vertically aligned Si NWs with the same length of 350 nm but different diameters of 350, 260, and 190 nm are shown in Fig. 4 a, b and c, respectively, while their corresponding current images obtained at the sample bias of − 1.5 V are presented in (d), (e), and (f). It should be noted, as the Cr/Pt-coated AFM tip is a wedge with a large angle, the Si NWs exhibit a larger diameter than their actual ones. Additionally, the current out of the nanowires could not be well detected as the tip may not be able to contact with the substrate, so only the currents measured on nanowires are taken into account. From the current images, it can be observed that most of the edges of Si nanowires exhibit a little better conductance than the center. This may be resulted by side contact between the AFM tip and the Si NW with a larger contact area. Additionally, due to the obvious roughness on the top surface, some regions at the center area may also show large current similar to the edge, resulting in no distinct ring-like current distribution. On the other hand, the conductance of Si NWs is obviously related to the nanowires' diameter. It can be seen that both the conductive area ratio of nanowires and the absolute current values increase significantly as the diameter decreases from 350 to 190 nm. The results suggest that the Si NWs with smaller diameters are more conductive than those with larger ones. To get the diameter dependence more intuitively, the current profiles along the marked lines in Fig. 4 d to f are displayed in Fig. 4g. It clearly shows that the Si NWs with the diameter of 190 nm are much more conductive than those with the diameters of 260 nm and 350 nm. Such diameter dependence can also be obtained from the statistical histograms of current distributions on Si NWs with different diameters, as shown in Additional file 1: Figure S1(a), which exhibits the current distribution shifts to high values when the diameter decreases. The averaged currents (I_{av}) of Si NWs

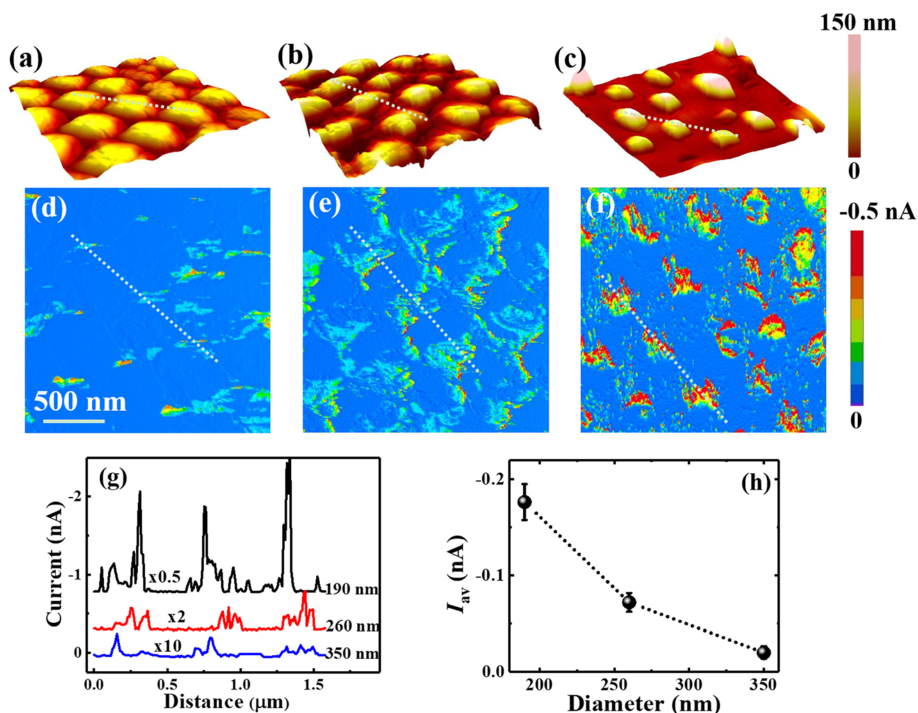

Fig. 4 The topography images of Si NWs with the same length of 350 nm but different diameters of **a** 350 nm, **b** 260 nm, **c** 190 nm. Their corresponding current images obtained under the sample bias of − 1.5 V are given in **d**, **e** and **f**, respectively. Current profiles along the marked lines in **d**–**f** are plotted in **g**, and **h** presents the averaged current (I_{av}) over the nanowires as a function of NWs' diameter. Corresponding lines are added in the topography images of **a**–**c** and the profile curves in **g** are vertically shifted for guidance

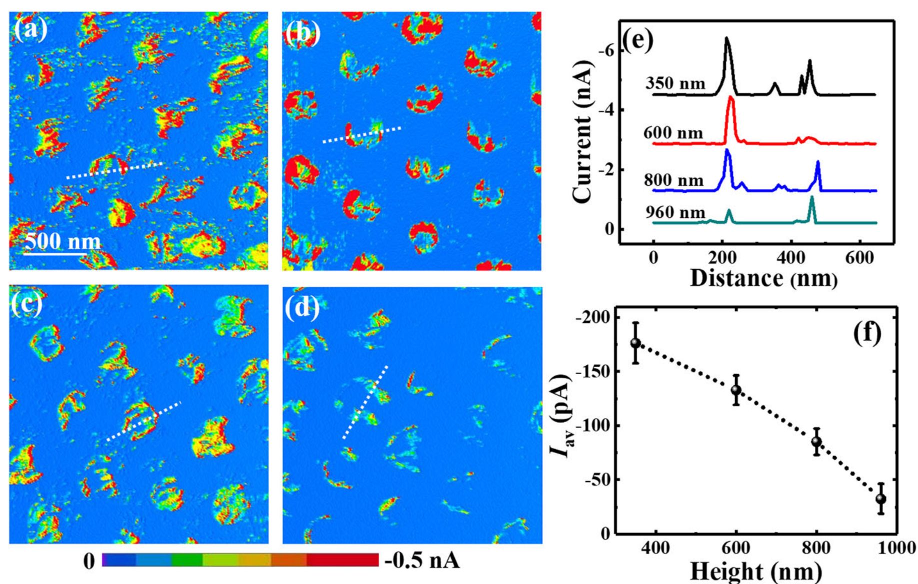

Fig. 5 The current images of Si NWs under the sample bias of − 1.5 V with the same diameter of 190 nm but different lengths of **a** 350 nm, **b** 600 nm, **c** 800 nm, and **d** 960 nm, respectively. The current profiles along the marked lines in **a**–**d** are plotted in **e**, and **f** presents the averaged currents of the nanowires (I_{av}) as a function of NWs' length. The profile curves in **e** are vertically shifted for guidance

are calculated by averaging the current over all the nanowires in the current images, which is plotted in Fig. 4h as a function of NWs' diameter. The averaged current of Si NWs exhibits a dramatical nine times increase when the NWs' diameter decreases from 350 to 190 nm. Similar current dependence on diameter has been achieved on single InAs nanowires as well as on single Si nanowire devices [35, 47].

Typical current images of Si NWs with different lengths and the same diameter of 190 nm measured at the sample bias of − 1.5 V are presented in Fig. 5. Figure 5 a to d show the current images of Si NWs with the lengths of 350, 600, 800, and 960 nm, respectively. It can be seen that in these current images, the conductive areas decrease obviously with the increasing length, while the decrease of absolute current is not so obvious, especially for the NWs with the length of 350 nm and 600 nm. Maybe due to the existence of local irregular surface roughness, even larger current was observed at some spots in Fig. 5b. Nevertheless, the average current of Fig. 5b was much smaller than that of Fig.5a. Using the same analyses as above, the current profiles along the marked lines are presented in Fig. 5e, and the statistical histograms are shown in Additional file 1: Figure S1(b). Both of them clearly exhibit a significant current decrease with the increased NWs' length. The averaged currents of the nanowires as a function of NWs' lengths are plotted in Fig. 5f, and they are on the order of tens to hundreds pA which is much smaller than that shown in Fig. 5 a to e on the order of nA. It is because that the nanowires exhibit relatively large current only at a few conductive spots when most regions are nonconductive. From Fig. 5f, the averaged current exhibits more than three times decrease when the length increases from 300 to 960 nm, indicating the nanowires' conductance decreasing with the increased length. The dependence of nanowire resistance on the length has previously been investigated by four-point resistance measurements on semiconductor nanowires, which suggested that under Ohmic contact the nanowire' resistance increased with its length linearly with the slope of resistivity [56, 57]. In our case, from the plot of I ~ 1/L as given in Additional file 1: Figure S2, the dependence is remarkably nonlinear; hence, the resistivity could not be correctly obtained from the curve slope. It is worth note in CAFM measurements, the total measured resistance includes the contact resistance between Cr/Pt-coated tips and Si NW ($R_{\text{tip/NW}}$), the resistance of Si NW (R_{NW}) and the resistance of Si wafers (R_{bulk}). Since the resistance measured by CAFM mainly comes from the localized surface area beneath the tip and it decreases quickly with the increased area along the current path, R_{bulk} is much smaller compared with R_{NW} and $R_{\text{tip/NW}}$. On the other hand, due to the very small metal-semiconductor contact area between the tip and nanowire, the contact resistance $R_{\text{tip/NW}}$ is much larger than the nanowire resistance R_{NW}. The nonlinearity of current dependence on 1/L just indicates the presence of large contact resistance. Therefore, in the measurements carried out by CAFM, metal-semiconductor contact resistance should be emphatically considered, in which the Schottky barrier plays an important role.

To verify the above inference, current-voltage (I–V) curves were recorded on individual Si NWs to investigate the Schottky barrier at the metal tip/Si nanowire contact. Typical I–V curves on the Si NWs with the same length of 350 nm but different diameters are presented in Fig. 6a and those on the Si NWs with the same diameter of 190 nm but different lengths are displayed in Fig. 6b, respectively. All the I–V curves exhibit larger currents at negative sample voltage region, in accordance with the typical I–V curves with the Schottky contact between the metal tip and n-type semiconductor. As the I–V curves exhibit good metal-semiconductor characteristics, it indicates that the oxygen layer effect on conductance is not serious and thus assumed minimal in the following discussion. Meanwhile, the results show that smaller and shorter nanowires exhibit larger conductance than larger and longer ones, well consistent with the results obtained from current images. For quantitative analyses, a well-known thermionic emission model for a metal-semiconductor contact is adopted [58, 59]. In this model, the I–V characteristics of a Schottky contact to n-type semiconductor in the presence of series resistance can be approximated as [59]:

$$I = I_S\left[\exp\left(\frac{q(V-IR_S)}{\mathrm{n}kT}\right)-1\right], \tag{1}$$

where n is the ideal factor and R_S is the series resistance. I_S is the saturation current, which can be expressed by:

$$I_S = \mathrm{AA}*T^2\ \exp\left(-\frac{\phi_B}{kT}\right), \tag{2}$$

where A is the contact area, A* is Richardson's constant, and ϕ_B is the Schottky barrier height (SBH) between the metal tip and Si nanowire. Thus, SBH can be obtained with the formula:

$$\phi_B = kT\ \ln\left(\frac{\mathrm{AA}*T^2}{I_S}\right), \tag{3}$$

The I–V curves in Fig. 6 a and b can be well fitted by Eq. (1), and a typical fitting line at the forward region is shown in the inset of Fig. 6a. To get the SBH values

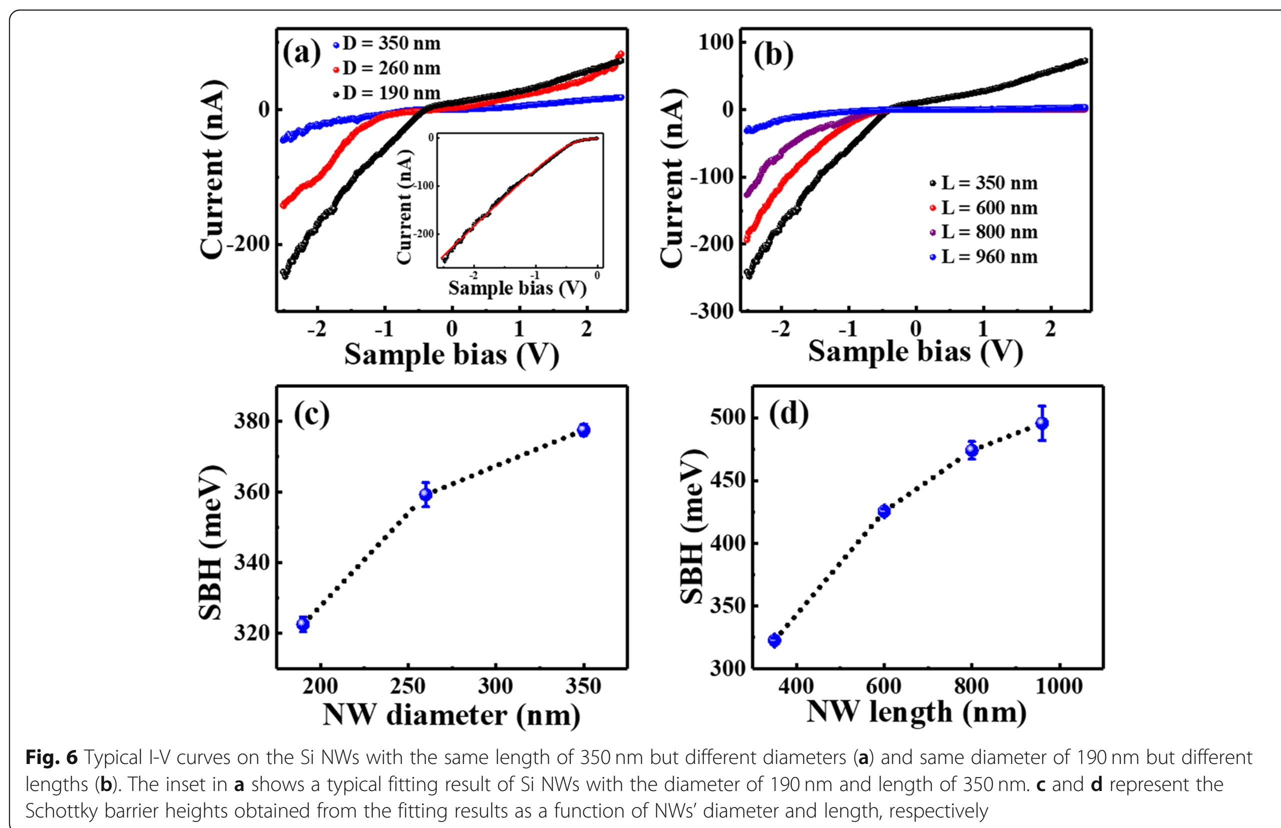

Fig. 6 Typical I-V curves on the Si NWs with the same length of 350 nm but different diameters (**a**) and same diameter of 190 nm but different lengths (**b**). The inset in **a** shows a typical fitting result of Si NWs with the diameter of 190 nm and length of 350 nm. **c** and **d** represent the Schottky barrier heights obtained from the fitting results as a function of NWs' diameter and length, respectively

from the saturation current, the effective Richardson constant A* is assumed to be approximately equal to that of bulk silicon, i.e., 112 A cm^{-2} K^{-2} for n-type silicon [59]. The contact area is assumed to be 2×10^{-11} cm^2 by taking the Cr/Pt-coated tip radius as 25 nm. The SBH values are obtained to be about 322, 359 and 377 meV for the Si NWs with the same length of 350 nm and different diameters of 190, 260 and 350 nm, respectively. For Si NWs with the same diameter of 190 nm and different lengths of 350, 600, 800 and 960 nm, the SBH values are 322, 425, 473 and 495 meV, correspondingly. For comparison, typical I–V curve was measured on the same type of Si wafer, as shown in Additional file 1: Figure S3(a). It clearly shows that the conductance of Si wafer is much smaller than the produced NWs. Detectable current could only be measured at high bias voltages (− 4 ~ − 10 V). After fitting the I–V curves with the above thermionic emission model (Additional file 1: Figure S3(b)), SBH value of 0.60 eV was obtained for bulk Si. Obviously, all of the measured SBH values for Si NWs with different diameters and lengths are smaller than that of the bulk Si. Similar Schottky barrier lowering in nanowires has been reported by different groups on different types of nanowires, which was attributed to the carrier recombination in depletion region [46, 60], barrier inhomogeneity and Joule heating effect [48], or image potential lowering [47]. In our case, the barrier lowering can be also attributed to the large density of surface states induced image potential lowering and carrier charging in depletion region.

The dependence of SBH values on nanowires' diameter and length is plotted in Fig. 6 c and d respectively, and it can be found that the SBH increases obviously with the increasing of both nanowires' diameter and length. In addition, the same measurements were done on Si NWs with different diameters of 260 and 350 nm for all lengths, and the I–V curves are shown in Additional file 1: Figure S4 a and b, respectively. The obtained diameter-dependent SBH values from curve fitting for all lengths are listed in Table 1 and plotted in Additional file 1: Figure S5. The results show that the SBH values increase with increased diameter for all lengths, and also increase with increased length for all diameters. Therefore, the results obtained from the I–V curves analyses suggest that the Schottky barrier lowering is more significant for the nanowires with smaller diameters and shorter lengths. On the other hand, the ideal factor *n* and series resistances *R*s of Si NWs with different diameters and lengths can also be obtained from the fitting results, as listed in Table 1. The results show that *n* is much larger than 1 for all nanowires (2.8 ~ 9.4), indicating that the contact between the tip and nanowire is not ideal metal-semiconductor contact, probably due to the existence of oxide layer. On the other hand, the *R*s increases with increased diameter as well as

Table 1 Schottky barrier height (SBH), ideal factor (*n*) and series resistance (*Rs*) obtained from the fitting results of I–V curves obtained on Si NWs with different diameters and lengths

Length & Diameter		SBH (meV)	*n*	*Rs* (MΩ)
L=350 nm	D = 190 nm	323	5.7	6.1
	D = 260 nm	359	6.8	9.2
	D = 350 nm	378	9.4	21.6
L=600 nm	D = 190 nm	426	5.0	6.7
	D = 260 nm	438	7.1	31.9
	D = 350 nm	446	5.5	40.3
L=800 nm	D = 190 nm	474	4.1	11.0
	D = 260 nm	489	9.4	36.7
	D = 350 nm	542	7.7	40.4
L=960 nm	D = 190 nm	496	4.7	32.3
	D = 260 nm	544	6.2	181.3
	D = 350 nm	567	2.8	288.0

increased length. For example, R_S increases from 6.1 to 21.6 MΩ as the diameter increases from 190 to 350 nm for the same length of 350 nm and increases from 6.1 to 32.3 MΩ for the length from 350 to 960 nm with the same diameter of 190 nm. The increase of *R*s with increased length is reasonable, while that increase with increased diameter is out of expectation. There is no good explanation for it at present, which may because that the series resistance is not simply the resistance of nanowire and the effective tip-nanowire contact area is not exactly equal to the nanowire's sectional area. Nevertheless, the series resistances of Si NWs did be much smaller than the contact resistances, therefore the conductance of Si NWs should be dominated by the SBH determined contact resistance.

The origin of the size-dependent SBH is not very clear yet. The mechanism explanation for similar diameter dependence of SBH has been supposed in several literatures [45–48, 60]. For example, Leonard et al. interpreted this effect with the point of electron-hole recombination in depletion region [60]. As the recombination time decreased as the nanowire diameter was reduced, current density increased with decreasing nanowire diameter. Yoon et al. explained the diameter-dependent SBH using the presence of interface states [47]. Mao et al. attributed its origin to barrier inhomogeneity and Joule heating effect [48]. In our case, the Si NWs are made by the MACE method, so there inevitably exist an amount of defects on the surface and a reformed thin oxygen layer, resulting in a large density of surface states. Actually, from the enlarged SEM images and AFM observation, the top surface of Si NWs is very rough, further increasing the density of surface states. We think the presence of surface (or interface) states should be the main cause of the diameter dependence of SBH. According to previous literatures [47, 61, 62], the SBH lowering was interpreted by charged interface states. By adopting the cylindrical coaxial capacitor model used in reference [47], interface state–induced carrier transfer will form two opposite charged layers (metal and semiconductor contact surface) which generates an electric field opposite to the built-in electric field and lowers the barrier potential. As the surface state density increases with decreased nanowire diameter, smaller SBH is obtained on nanowires with a smaller diameter. Why the values of SBH related to the nanowire length is not clear yet. As the MACE time increased, the surface disorder or roughness increases correspondingly. Different changes in the surface microstructures may introduce different changes of SBH values, which need further investigations to work it out. Anyway, whatever the origin of size dependence of conductive properties, the size-dependent SBH lowering could result in higher conductance, which should be beneficial for practical applications.

EFM Measurements on Single Si NWs

To further verify the size-dependent SBH results of Si NWs obtained by CAFM, the EFM measurements were performed on the same samples and the EFM phase shift was measured as a function of applied DC bias. In previous literatures [63, 64], the relation between phase shift and electrostatic force has already been established, where the tip-sample system is roughly treated as a plane capacitor. When a bias is applied between the tip and the sample, the capacitive electrostatic force gradient would cause a phase shift. At a lifted height where the Van de Waals force can be ignored, the electrostatic force acted on the tip can be expressed as [63]:

$$F = \frac{1}{2}\frac{\partial C}{\partial z}\left(V_{EFM} - V_{CPD}\right)^2, \quad (4)$$

where C, V_{EFM}, and V_{CPD} are the capacitance, applied DC voltage and contact potential difference (CPD) between the sample and tip, respectively. V_{CPD} can be written as $(\boldsymbol{\phi}_{\mathrm{sample}} - \boldsymbol{\phi}_{\mathrm{tip}})/e$ when the bias voltage V_{EFM} was applied to the sample in our experiments. The phase shift detected by EFM is proportional to the gradient of the electrostatic force, which can be written as:

$$\Delta\Phi = -\frac{Q}{k}\frac{\partial F}{\partial z} = -\frac{Q}{k}\left[\frac{1}{2}\frac{\partial^2 C}{\partial z^2}\left(V_{EFM} - V_{CPD}\right)^2\right], \quad (5)$$

where Q is the quality factor, k is the spring constant of the probe and z is the distance between tip and top of Si NW.

From Eq. (5), it can be seen that the EFM phase shift should be equal to zero at $V_{\mathrm{EFM}} = V_{\mathrm{CPD}}$. Therefore, V_{CPD} can be achieved from the EFM measurements. The $\Delta\Phi \sim V_{\mathrm{EFM}}$ curves measured at a lift height of 100 nm on

the individual Si NWs with different diameters and lengths are shown in Fig. 7 a and b as the scattered dots, respectively. By using Eq. (5), the $\Delta\Phi \sim V_{\mathrm{EFM}}$ curves can be fitted well, shown as the solid lines in Fig. 7 a and b. From the fitting parameters, the values of V_{CPD} can be obtained, as presented in Fig. 7 c and d as a function of diameter and length respectively. The results show that the CPD values increase with increased diameter and increased length. Similar CPD results have been reported in a previous work performed by Kelvin probe force microscopy on ZnO NWs, in which the absolute value of CPD between ZnO nanowire and Pt/Ir tip also increased with increased diameter [65]. As diagrammed in Additional file 1: Figure S6, the value of SBH roughly equals to qV_{CPD} plus E_{n} (= $E_{\mathrm{C}} - E_{\mathrm{F}}$). As E_{n} is a constant for all Si NWs made from the same material, the size dependence of V_{CPD} well represents the size dependence of SBH. Therefore, from the EFM results, it can be suggested that, the SBH values increase with the increasing of NWs' diameter and length, well consistent with the results achieved by CAFM measurements. Similarly, the EFM measurements are performed on all series of Si NWs, and the diameter-dependent V_{CPD} values at different lengths are shown in Additional file 1: Figure S7(a) and (b) respectively, which exhibit same diameter dependence as that obtained by CAFM.

Conclusion

In summary, by a simple, low-cost method without involving any intricated procedures, Si NWs arrays with controllable diameters and lengths are prepared. Both the diameter and length of SiNWs can be well controlled by adjusting the etching time. The conductive properties include the current map and I–V curves are directly measured on individual Si NWs without complex nanofabrication procedure by the means of CAFM. Size-dependent conductance of Si NWs can be obtained from both the current images and I–V curves. Our results demonstrate that the Si NWs with a smaller diameter and shorter length exhibit better conductance. It can be attributed to the size dependence of SBH, which increased from 322 to 377 meV with the diameter increasing from 190 to 350 nm for the same length of 350 nm. Correspondingly, the SBH values increased from 322 to 495 meV as the length varies from 350 to 960 nm for the same diameter of 190 nm. The same size-dependent SBH can also be obtained from the EFM measurements. Such SBH lowering is interpreted by charged interface states. Therefore, our study not only reveals the size-dependent properties of Si NWs but also suggests that CAFM can act as an effective means to explore the size (or other parameters) dependence of conductive properties on individual nanostructures.

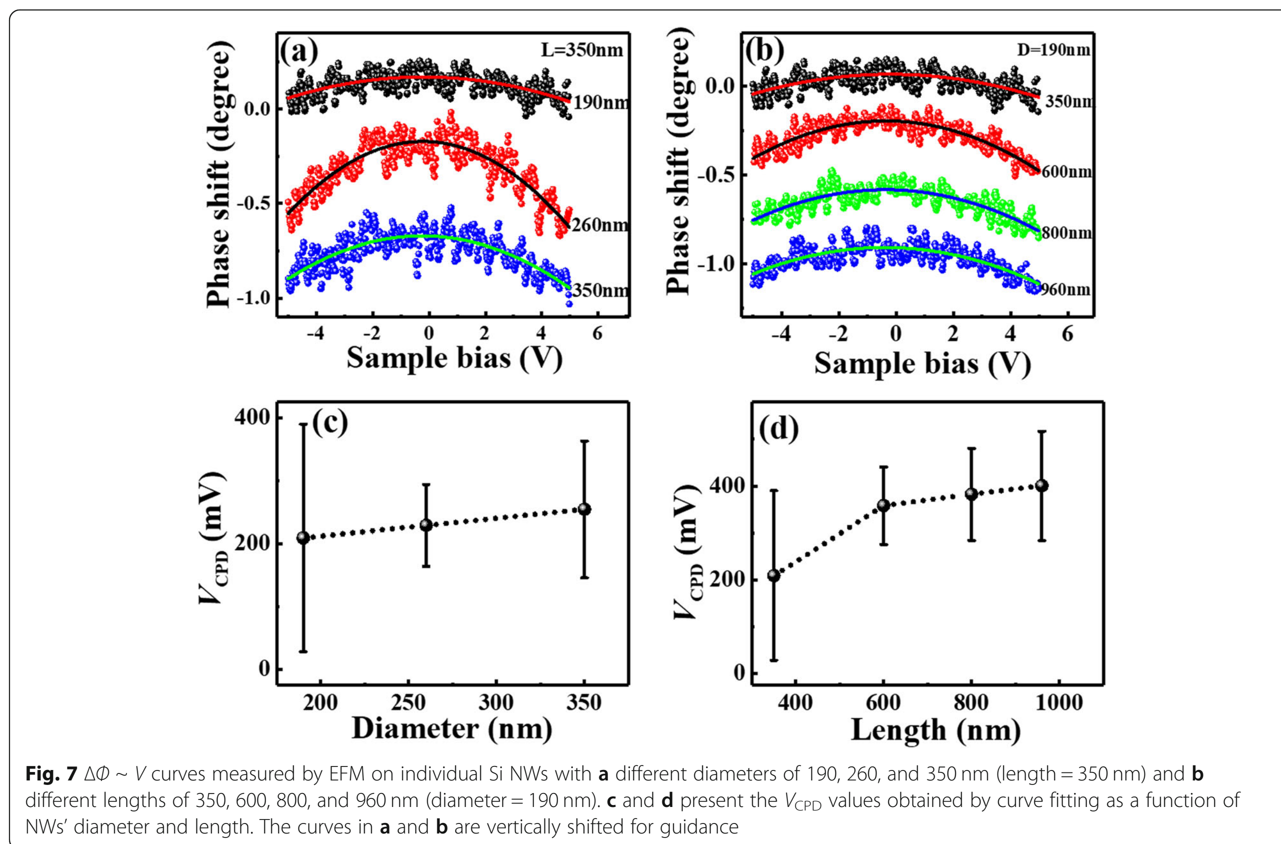

Fig. 7 $\Delta\Phi \sim V$ curves measured by EFM on individual Si NWs with **a** different diameters of 190, 260, and 350 nm (length = 350 nm) and **b** different lengths of 350, 600, 800, and 960 nm (diameter = 190 nm). **c** and **d** present the V_{CPD} values obtained by curve fitting as a function of NWs' diameter and length. The curves in **a** and **b** are vertically shifted for guidance

Supplementary information

Supplementary information accompanies this paper at https://doi.org/10.1186/s11671-020-3277-3.

Additional file 1: Figure S1. Histograms of the current distribution of Si NWs obtained from the current images as shown in Figures 3 and 4. (a) and (b) presents the statistical current distributions of Si NWs with different diameters (same length of 350 nm) and different lengths (same diameter of 190 nm), respectively. The current distribution shifts to right with decreased diameter and length. **Figure S2.** Averaged current as a function of 1/Length. **Figure S3.** (a) Typical I-V curve measured on the same type of Si wafer; (b) Fitting result of the I-V curve in (a) with equation (1). **Figure S4.** Typical I-V curves on the Si NWs with different lengths and the same diameter of 260 nm (a) and 350 nm (b), respectively. The curves exhibit similar length dependence as that obtained from Fig. 6b. **Figure S5.** Diameter and length dependent Schottky barrier heights obtained from the fitting results of I-V curves on Si NWs with different lengths and different diameters are shown in (a) and (b), respectively. **Figure S6.** Energy band diagram of the contact interface between metallic tip and Si NW. V_{CPD} is the contact potential difference and the value of SBH roughly equals to the sum of qV_{CPD} and E_n. **Figure S7.** Diameter and length dependent contact potential difference values obtained by EFM curve fitting are given in (a) and (b), respectively.

Abbreviations

CAFM: Conductive atomic force microscopy; CPD: Contact potential difference; EFM: Electrostatic force microscopy; MACE: Metal-assisted chemical etching; NSL: Nanosphere lithography; PS: Polystyrene spheres; RIE: Reactive ion etching; SBH: Schottky barrier height; SEM: Scanning electron microscopy; Si NWs: Si nanowires; SPM: Scanning probe microscopy

Acknowledgements

The RIE and Raman experiments were carried out in Fudan Nanofabrication Laboratory.

Authors' Contributions

XFH carried out the experiments. SJL and JW participated in Raman and SEM experiments. XFH and XJY interpreted the results and wrote the manuscript. ZMJ helped in interpretation and discussions. All authors read and approved the final manuscript.

Funding

This work was supported by the Natural Science Foundation of Shanghai (No. 17ZR1402600).

Availability of Data and Materials

The datasets used for supporting the conclusion are included in the article and the supporting file.

Competing Interests

The authors declare that they have no competing interests.

Received: 12 October 2019 Accepted: 4 February 2020
Published online: 02 March 2020

References

1. Sivakov V, Andrä G, Gawlik A, Berge A, Plentz J, Falk F, Christiansen SH (2009) Silicon nanowire-based solar cells on glass: synthesis, optical properties, and cell parameters. Nano Lett 9(4):1549–1554
2. Garnett E, Yang P (2010) Light trapping in silicon nanowire solar cells. Nano Lett 10(3):1082–1087
3. Ge M, Rong J, Fang X, Zhou C (2012) Porous doped silicon nanowires for lithium ion battery anode with long cycle life. Nano Lett 12(5):2318–2323
4. Wang Y, Wang T, Da P, Xu M, Wu H, Zheng G (2013) Silicon nanowires for biosensing, energy storage, and conversion. Adv Mater 25(37):5177–5195
5. Hochbaum AI, Chen R, Delgado RD, Liang W, Garnett EC, Najarian M, Majumdar A, Yang P (2008) Enhanced thermoelectric performance of rough silicon nanowires. Nature 451(7175):163–167
6. Schmidt V, Wittemann JV, Senz S, Gösele U (2009) Silicon nanowires: a review on aspects of their growth and their electrical properties. Adv Mater 21(25–26):2681–2702
7. Ramanujam J, Shiri D, Verma A (2011) Silicon nanowire growth and properties: a review. Mater Express 1(2):105–126
8. Wang Y, Schmidt V, Senz S, Gosele U (2006) Epitaxial growth of silicon nanowires using an aluminium catalyst. Nat Nanotechnol 1(3):186–189
9. Hofmann S, Ducati C, Neill RJ, Piscanec S, Ferrari AC, Geng J, Dunin-Borkowski RE, Robertson J (2003) Gold catalyzed growth of silicon nanowires by plasma enhanced chemical vapor deposition. J Appl Phys 94(9):6005–6012
10. Büttner CC, Zakharov ND, Pippel E, Gösele U, Werner P (2008) Gold-enhanced oxidation of MBE-grown silicon nanowires. Semicond Sci Technol 23(7):15501
11. Park I, Li Z, Pisano AP, Williams RS (2010) Top-down fabricated silicon nanowire sensors for real-time chemical detection. Nanotechnology 21(1): 015501
12. Juhasz R, Elfström N, Linnros J (2005) Controlled fabrication of silicon nanowires by electron beam lithography and electrochemical size reduction. Nano Lett 5(2):275–280
13. Hsu C-M, Connor ST, Tang MX, Cui Y (2008) Wafer-scale silicon nanopillars and nanocones by Langmuir–Blodgett assembly and etching. Appl Phys Lett 93(13):133109
14. Kang Y, Wang D, Wang P, Chen A, Li H, Wang X, Yang J (2018) Diameter dependence of the UV light detecting performance of InGaN/GaN nanorods array photodetector. Micro Nano Lett 13(10): 1437–1442
15. Huang Z, Geyer N, Werner P, de Boor J, Gosele U (2011) Metal-assisted chemical etching of silicon: a review. Adv Mater 23(2):285–308
16. Han H, Huang Z, Lee W (2014) Metal-assisted chemical etching of silicon and nanotechnology applications. Nano Today 9(3):271–304
17. Kim SM, Khang DY (2014) Bulk micromachining of Si by metal-assisted chemical etching. Small 10(18):3761–3766
18. Azeredo BP, Sadhu J, Ma J, Jacobs K, Kim J, Lee K, Eraker JH, Li X, Sinha S, Fang N, Ferreira P, Hsu K (2013) Silicon nanowires with controlled sidewall profile and roughness fabricated by thin-film dewetting and metal-assisted chemical etching. Nanotechnology 24(22):225305
19. Balasundaram K, Sadhu JS, Shin JC, Azeredo B, Chanda D, Malik M, Hsu K, Rogers JA, Ferreira P, Sinha S, Li X (2012) Porosity control in metal-assisted chemical etching of degenerately doped silicon nanowires. Nanotechnology 23(30):305304
20. Chartier C, Bastide S, Lévy-Clément C (2008) Metal-assisted chemical etching of silicon in HF–H_2O_2. Electrochim Acta 53(17):5509–5516
21. Qu Y, Liao L, Li Y, Zhang H, Huang Y, Duan X (2009) Electrically conductive and optically active porous silicon nanowires. Nano Lett 9(12):4539–4543
22. Zhang T, Wu S, Xu J, Zheng R, Cheng G (2015) High thermoelectric figure-of-merits from large-area porous silicon nanowire arrays. Nano Energy 13: 433–441
23. Feser JP, Sadhu JS, Azeredo BP, Hsu KH, Ma J, Kim J, Seong M, Fang NX, Li X, Ferreira PM, Sinha S, Cahill DG (2012) Thermal conductivity of silicon nanowire arrays with controlled roughness. J Appl Phys 112(11):114306
24. Peng K-Q, Wang X, Li L, Hu Y, Lee S-T (2013) Silicon nanowires for advanced energy conversion and storage. Nano Today 8(1):75–97
25. Eichfeld SM, Ho T-T, Eichfeld CM, Cranmer A, Mohney SE, Mayer TS, Redwing JM (2007) Resistivity measurements of intentionally and unintentionally template-grown doped silicon nanowire arrays. Nanotechnology 18(31):315201
26. Swinkels MY, van Delft MR, Oliveira DS, Cavalli A, Zardo I, van der Heijden RW, Bakkers EPAM (2015) Diameter dependence of the thermal conductivity of InAs nanowires. Nanotechnology 26(38):385401
27. Chen K-I, Li B-R, Chen Y-T (2011) Silicon nanowire field-effect transistor-based biosensors for biomedical diagnosis and cellular recording investigation. Nano Today 6(2):131–154
28. Boukai AI, Bunimovich Y, Tahir-Kheli J, Yu JK, Goddard WA 3rd, Heath JR (2008) Silicon nanowires as efficient thermoelectric materials. Nature 451(7175):168–171
29. Hussain S, Xu K, Ye S, Lei L, Liu X, Xu R, Xie L, Cheng Z (2019) Local electrical characterization of two-dimensional materials with functional atomic force microscopy. Front Physiol 14(3):33401
30. Hui F, Lanza M (2019) Scanning probe microscopy for advanced nanoelectronics. Nature Electron 2(6):221–229

31. Liu J, Goswami A, Jiang K, Khan F, Kim S, McGee R, Li Z, Hu Z, Lee J, Thundat T (2018) Direct-current triboelectricity generation by a sliding Schottky nanocontact on MoS2 multilayers. Nat Nanotechnol 13(2):112–116
32. Lanza M (ed) (2017) ISBN: 978–3–527-34091-0, Publisher) Conductive Atomic Force Microscopy:Application in Nanomaterials. Wiley-VCH, Weinheim
33. Lee JA, Lim YR, Jung CS, Choi JH, Im HS, Park K, Park J, Kim GT (2016) Schottky nanocontact of one-dimensional semiconductor nanostructures probed by using conductive atomic force microscopy. Nanotechnology 27(42):425711
34. Du W, Yang X, Pan H, Ji X, Ji H, Luo S, Zhang X, Wang Z, Yang T (2016) Controlled-direction growth of planar InAsSb nanowires on Si substrates without foreign catalysts. Nano Lett 16(2):877–882
35. Yang T, Hertenberger S, Morkötter S, Abstreiter G, Koblmüller G (2012) Size, composition, and doping effects on in (Ga) as nanowire/Si tunnel diodes probed by conductive atomic force microscopy. Appl Phys Lett 101(23): 233102
36. Tang C, Jiang C, Bi S, Song J (2016) Photoelectric property modulation by nanoconfinement in the longitude direction of short semiconducting nanorods. ACS Appl Mater Interfaces 8(17):11001–11007
37. Alvarez J, Ngo I, Gueunier-Farret ME, Kleider JP, Yu L, Cabarrocas PR, Perraud S, Rouviere E, Celle C, Mouchet C, Simonato JP (2011) Conductive-probe atomic force microscopy characterization of silicon nanowire. Nanoscale Res Lett 6(1):110
38. Xia H, Lu Z-Y, Li T-X, Parkinson P, Liao Z-M, Liu F-H, Lu W, Hu W-D, Chen P-P, Xu H-Y, Zou J, Jagadish C (2012) Distinct photocurrent response of individual GaAs nanowires induced by n-type doping. ACS Nano 6(7):6005–6013
39. Barreda JL, Keiper TD, Zhang M, Xiong P (2017) Multiple schottky barrier-limited field-effect transistors on a single silicon nanowire with an intrinsic doping gradient. ACS Appl Mater Interfaces 9(13):12046–12053
40. Lee SJ (2009) Size dependence of the transport properties of silicon nanostructures. J Korean Phys Soc 55(6):2491–2495
41. Niebelschütz M, Cimalla V, Ambacher O, Machleidt T, Ristic J, Calleja E (2007) Electrical performance of gallium nitride nanocolumns. Phys E 37(1–2):200–203
42. Vaurette F, Nys JP, Deresmes D, Grandidier B, Stiévenard D (2008) Resistivity and surface states density of n- and p-type silicon nanowires. J Vac Sci Technol B: Microelectron Nanometer Structures 26(3):945
43. Calarco R, Marso M, Richter T, Aykanat AI, Meijers R, Avd H, Stoica T, Lüth H (2005) Size-dependent photoconductivity in MBE-grown GaN–nanowires. Nano Lett 5(5):981–984
44. Ou X, Geyer N, Kögler R, Werner P, Skorupa W (2011) Acceptor deactivation in individual silicon nanowires: from thick to ultrathin. Appl Phys Lett 98(25): 253103
45. Calahorra Y, Yalon E, Ritter D (2015) On the diameter dependence of metal-nanowire Schottky barrier height. J Appl Phys 117(3):034308
46. Soudi A, Hsu CH, Gu Y (2012) Diameter-dependent surface photovoltage and surface state density in single semiconductor nanowires. Nano Lett 12(10):5111–5116
47. Yoon K, Hyun JK, Connell JG, Amit I, Rosenwaks Y, Lauhon LJ (2013) Barrier height measurement of metal contacts to Si nanowires using internal photoemission of hot carriers. Nano Lett 13(12):6183–6188
48. Mao S, Shang T, Park B, Anderson DD, Dillon SJ (2014) Measuring size dependent electrical properties from nanoneedle structures: Pt/ZnO Schottky diodes. Appl Phys Lett 104(15):153105
49. Li B, Niu G, Sun L, Yao L, Wang C, Zhang Y (2018) Design optimization and antireflection of silicon nanowire arrays fabricated by au-assisted chemical etching. Mater Sci Semicond Process 82:1–8
50. Huang S, Zhang H, Wu Z, Kong D, Lin D, Fan Y, Yang X, Zhong Z, Huang S, Jiang Z, Cheng C (2014) Large-area ordered P-type Si nanowire arrays as photocathode for highly efficient photoelectrochemical hydrogen generation. ACS Appl Mater Interfaces 6(15):12111–12118
51. Zhang M-L, Peng K-Q, Fan X, Jie J-S, Zhang R-Q, Lee S-T, Wong N-B (2008) Preparation of large-area uniform silicon nanowires arrays through metal-assisted chemical etching. J Phys Chem C 112(12):4444–4450
52. Chen H, Zou R, Chen H, Wang N, Sun Y, Tian Q, Wu J, Chen Z, Hu J (2011) Lightly doped single crystalline porous Si nanowires with improved optical and electrical properties. J Mater Chem 21:801–805
53. Widulle F, Ruf T, Konuma M, Silier I, Cardona M, Kriegseis W, Ozhogin VI (2001) Isotope effects in elemental semiconductors:a Raman study of silicon. Solid State Commun 118(2001):1–22
54. Lajvardi M, Eshghi H, Ghazi ME, Izadifard M, Goodarzi A (2015) Structural and optical properties of silicon nanowires synthesized by Ag-assisted chemical etching. Mater Sci Semicond Process 40:556–563
55. Lin G-R, Lin Y-H, Pai Y-H, Meng F-S (2011) Si nanorod length dependent surface Raman scattering linewidth broadening and peak shift. Opt Express 19(2):597–605
56. Motayed A, Davydov AV, Vaudin MD, Levin I, Melngailis J, Mohammad SN (2006) Fabrication of GaN-based nanoscale device structures utilizing focused ion beam induced Pt deposition. J Appl Phys 100(2):024306
57. Cossuet T, Donatini F, Lord AM, Appert E, Pernot J, Consonni V (2018) Polarity-dependent high electrical conductivity of ZnO nanorods and its relation to hydrogen. J Phys Chem C 122(39):22767–22775
58. Park JY, Lee H, Renzas JR, Zhang Y, Somorjai GA (2005) Probing hot electron flow generated on Pt nanoparticles with AuTiO2 Schottky fiodes during catalytic CO oxidation. Nano Lett 8(8):2388–2392
59. Yang Z, Du K, Wang H, Lu F, Pang Y, Wang J, Gan X, Zhang W, Mei T, Chua SJ (2019) Near-infrared photodetection with plasmon-induced hot electrons using silicon nanopillar array structure. Nanotechnology 30(7):075204
60. Leonard F, Talin AA, Swartzentruber BS, Picraux ST (2009) Diameter-dependent electronic transport properties of au-catalyst/Ge-nanowire Schottky diodes. Phys Rev Lett 102(10):106805
61. Koren E, Berkovitch N, Azriel O, Boag A, Rosenwaks Y, Hemesath ER, Lauhon LJ (2011) Direct measurement of nanowire Schottky junction depletion region. Appl Phys Lett 99(22):223511
62. Piscator J, Engström O (2008) Schottky barriers on silicon nanowires influenced by charge configuration. Appl Phys Lett 104(5):054515
63. Wu S, Wu Z, Lin D, Zhong Z, Jiang Z, Yang X (2014) Photogenerated charges and surface potential variations investigated on single Si nanorods by electrostatic force microscopy combined with laser irradiation. Nanoscale Res Lett 9(1):245
64. Lei CH, Das A, Elliott M, Macdonald JE (2004) Quantitative electrostatic force microscopy-phase measurements. Nanotechnology 15(5):627–634
65. Wang Z, Gu Y, Qi J, Lu S, Li P, Lin P, Zhang Y (2015) Size dependence and UV irradiation tuning of the surface potential in single conical ZnO nanowires. RSC Adv 5(52):42075–42080

Publisher's Note

Springer Nature remains neutral with regard to jurisdictional claims in published maps and institutional affiliations.

Submit your manuscript to a SpringerOpen journal and benefit from:

- ► Convenient online submission
- ► Rigorous peer review
- ► Open access: articles freely available online
- ► High visibility within the field
- ► Retaining the copyright to your article

Submit your next manuscript at ► springeropen.com